Redesign of *Schistosoma mansoni* NAD+ catabolizing enzyme : the active site H103W mutation restores ADP-ribosyl cyclase activity[†]

Isabelle Kuhn[§], **Esther Kellenberger**[§], **Didier Rognan**[§], **Frances E. Lund**[||], **Hélène Muller-Steffner**[§], and **Francis Schuber**[§,*]

Institut Gilbert Laustriat, UMR 7175 CNRS – Université Louis Pasteur (Strasbourg I), Faculté de Pharmacie, 67401 Illkirch, France and Trudeau Institute, Saranac Lake NY 12983, USA

Abstract

Schistosoma mansoni NAD(P)+ catabolizing enzyme (*Sm*NACE) is a new member of the ADP-ribosyl cyclase family. In contrast to all the other enzymes which are involved in the production of metabolites that elicit Ca^{2+} mobilization, *Sm*NACE is virtually unable to transform NAD+ into the second messenger cyclic ADP-ribose (cADPR). Sequence alignments revealed that one of four conserved residues within the active site of these enzymes was replaced in *Sm*NACE by a histidine (His^{103}) instead of the highly conserved tryptophan. To find out whether the inability of *Sm*NACE to catalyze the canonical ADP-ribosyl cyclase reaction is linked to this change we have replaced His^{103} with a tryptophan. The H103W mutation in *Sm*NACE was indeed found to restore ADP-ribosyl cyclase activity as cADPR amounts for 7% of the reaction products, i.e., a value larger than observed for other members of this family such as CD38. Introduction of a Trp^{103} residue provides some of the binding characteristics of mammalian ADP-ribosyl cyclases such as increased affinity for Cibacron blue and slow-binding inhibition by araF-NAD+. Homology modeling of wild-type and H103W mutant three-dimensional structures, and docking of substrates within the active sites, provide new insight into the catalytic mechanism of *Sm*NACE. Both residue side chains share similar roles in the nicotinamide-ribose bond cleavage step leading to an E.ADP-ribosyl reaction intermediate. They diverge however in the evolution of this intermediate; His^{103} provides a more polar environment favoring the accessibility to water and hydrolysis leading to ADP-ribose at the expense of the intramolecular cyclization pathway resulting in cADPR.

CD38, which is expressed by cells isolated from many mammalian species, is a 'multifunctional' bitopic ecto-enzyme that catalyzes the transformation of NAD+ into ADPR[1] (NAD+glycohydrolase activity) and cADPR (ADP-ribosyl cyclase activity) (1,2). In addition, CD38 also hydrolyzes cADPR into ADPR (cADPR hydrolase activity) and produces pyridinium analogues of NAD(P)+, such as NAADP+, by a transglycosidation reaction (reviewed in 2,3). CD38 is remarkable in that it transforms NAD(P)+ into one or more calcium-mobilizing metabolites (4). Like CD38, the GPI-anchored ecto-enzyme CD157 can catalyze

[1]Abbreviations: *Sm*NACE, *Schistosoma mansoni* NAD(P)+ catabolizing enzyme; ADPR, ADP-ribose; cADPR, cyclic ADP-ribose; cGDPR, cyclic GDP-ribose; araF-NAD+, nicotinamide 2′-deoxy-2′-fluoroarabinoside adenine dinucleotide; RMS, root mean square; WT, wild type.

similar metabolic reactions (5). However, neither CD38 nor CD157 are particularly efficient cyclases as they produce only low levels of cADPR (about 1-3% of the reaction products). In contrast to these membrane-bound mammalian enzymes, the hydrosoluble ADP-ribosyl cyclase isolated from *Aplysia californica*, produces almost entirely cADPR from NAD$^+$ (6) and makes, under standard conditions, very little ADPR (7). Despite the apparent differences in the catalytic properties of CD38, CD157 and the *Aplysia* cyclase, an unifying partitioning reaction mechanism has been suggested for this family of enzymes (Figure 1). This mechanism proposes that the cleavage of the nicotinamide-ribose bond of NAD$^+$ leads to the formation of a common E·ADP-ribosyl intermediate. This intermediate then evolves to the reaction products through competing pathways: i) a macroscopically irreversible intermolecular reaction with water yielding ADPR, and ii) a reversible intramolecular reaction that gives cADPR (8,9). In the presence of an excess of alternative acceptors such as pyridines or methanol, transglycosidation and methanolysis can also be observed (3).

We have previously proposed that the preference of the E·ADP-ribosyl intermediate to undergo hydrolysis/solvolysis or cyclization depends on the structure of the particular enzyme within the ADP-ribosyl cyclase family (3). Therefore, to better understand the mode of action of this family of enzymes at a molecular level it is of great interest to identify the active site residues that direct the transformation of NAD$^+$ towards hydrolysis versus cyclization. The crystallographic structures of *A. californica* ADP-ribosyl cyclase (10), human CD157 (11) and human CD38 (12) are now known and, in combination with site-directed mutagenesis studies, they have yielded important clues regarding the role for particular residues within the active site. Overall, these enzymes have very similar three dimensional structures, including the architecture their active sites. Three key residues in the active site of human CD38 are involved in either catalysis (Glu^{226}) (9) and/or in the binding/positioning of the substrate within the active site (Trp^{125} and Trp^{189}) (13). These residues are conserved in all the different *Aplysia* ADP-ribosyl cyclases, CD38 and CD157 family members. A fourth residue, Glu^{146}, was shown to influence the balance between cyclization and hydrolysis in human (14) and mouse CD38 (15). This residue is conserved in all CD38 and *Aplysia* cyclase family members, however it is replaced e.g. by a Ser in the human CD157 (Figure 2). The molecular mechanism of the reactions catalyzed by the ADP-ribosyl cyclases (Figure 1B), i.e. the chemical nature of the transition state of the scissile bond cleavage in NAD$^+$ and of the ADP-ribosyl intermediate, and the role of the two Glu residues present in the active site of CD38 and *Aplysia* cyclases, has been discussed recently (3).

Recently we cloned the newest member of the ADP-ribosyl cyclase family from *Schistosoma mansoni*, that we named NACE (i.e., **NA**D(P)$^+$ **C**atabolizing **E**nzyme). *Sm*NACE showed significant structural and functional analogy to the other members of this enzyme family (16). However, in stark contrast to all these enzymes, *Sm*NACE is almost exclusively a NAD$^+$glycohydrolase and is essentially unable to catalyze the formation of cADPR (< 0.02 % of reaction products) from NAD$^+$. This is despite the fact that *Sm*NACE is able to convert the surrogate substrate NGD$^+$ (17) into cGDPR in high yield (16). Analysis of the putative active site of this enzyme, obtained by homology modeling, revealed that three of the four key residues described above for CD38 and ADP-ribosyl cyclase were strictly conserved: Glu^{124}, contained within the 'signature region', Trp^{165} and the catalytic Glu^{202} (Figure 2). However the second tryptophan (Trp^{125} in human CD38), which is highly conserved throughout this family of enzymes, is replaced by His^{103} in *Sm*NACE. Furthermore, in a putative *Schistosoma japonicum* NACE (Accession No AY222890) (18), this highly conserved Trp residue is also replaced by a histidine (His^{96}; Figure 2), suggesting that this exchange of residues might have a functional role in the schistosome enzymes. In the present work we produced a H103W mutant for *S. mansoni* NACE and studied the catalytic properties of this mutant to determine whether changing this residue would restore ADP-ribosyl cyclase activity in *Sm*NACE.

EXPERIMENTAL PROCEDURES

Site-directed Mutagenesis of SmNACE

The H103W mutant was constructed by PCR (PfuTurbo polymerase; Stratagene) using the pPICZαA vector (Invitrogen) containing solNACE cDNA as template (16). SolNACE cDNA encodes the hydrosoluble ecto-domain of *Sm*NACE (residues 20-275) which lacks the 5′ leader and 3′ GPI-anchor sequences of the original full length *Sm*NACE (16). A *myc*-epitope fused to a His_6-tag was introduced at the C-terminus of this construct to facilitate purification of the recombinant protein. The H in position 103 (CAC) was changed into a W (TGG) using the following oligonucleotide primers (mutated bases in bold): forward, 5′-AGCAGTACTTC***TGG***AGCCAGGTGATG-3′ and reverse 5′-CATCACCTGGCT***CCA***GAAGTACTGCT-3′. The technique used was adapted from the QuickChange multi-site directed mutagenesis kit (Stratagene). The mutation was verified by DNA sequencing of the clones using the 5′ and 3′ AOX primers (Invitrogen). The selected plasmid was then used to transform *Pichia pastoris* GS115 (his4) or SMD1163 (his4, pep4, prb1) strains (Invitrogen) according to the manufacturer's instructions.

Expression and Purification of the Recombinant Proteins

Clones of yeast transformed with the expression plasmids (pPICZαA/*Sm*NACE and those carrying the H103W mutation in the *Sm*NACE sequence) were grown overnight at 30°C in 10 mL of BMGY (Invitrogen). The cells were then harvested and resuspended in 5 mL BMMY/casamino acids (BMGY containing 0.5% v/v methanol instead of glycerol and 1% w/v casamino acids) (19). For the mutant, this induction medium was supplemented with 1.0 mM EDTA and 0.2 mM PMSF. After 24 h, 0.5% methanol was again added and the cultures were stopped after 48 h. The cells were then harvested and the enzymatic activities were tested in the supernatants. The clone that gave the highest yields in recombinant enzyme was selected for a scale-up. To that end, a 5 mL overnight starter culture was inoculated to flasks containing 100 mL BMGY and grown until reaching an $OD_{600} = 25$. The cells were then harvested and resuspended in 50 mL BMMY/1% w/v casamino acids supplemented or not (see above) with 1.0 mM EDTA and 0.2 mM PMSF. After 24 h 0.5% v/v methanol was again added and induction was stopped after 48 h.

After centrifugation the supernatant was dialyzed against 10 mM potassium phosphate buffer, pH 7.4 (Buffer A) and the proteins were loaded on a 5 mL Blue Sepharose 6 Fast Flow CL-6B (Amersham Biosciences) column. The recombinant *Sm*NACE was eluted with a 0–1.5 M NaCl linear gradient in Buffer A. This step yielded a wild-type enzyme of high purity (> 95%). The purification of the mutant, which was expressed at lower yield, necessitated an additional chromatography step on a Ni^{2+}-affinity column. The enzyme, previously dialyzed against a 100 mM potassium phosphate buffer, pH 8.0, containing 300 mM NaCl (Buffer B), was loaded on a Hi-Trap™ Chelating HP (Amersham Biosciences) column (1 mL), pre-equilibrated with a 50 mM solution of $NiSO_4$ in water followed by Buffer B. The column then was washed with Buffer B containing 10 mM imidazole and the H103W mutant of recombinant *Sm*NACE containing the His_6-sequence was eluted with a linear gradient of 10-500 mM imidazole in Buffer B. The collected fractions containing the enzyme were pooled and dialyzed against Buffer A. To avoid cross-contamination, separate affinity columns were used for WT and mutant *Sm*NACE. The protein concentration was determined by the protein BCA assay (Pierce) using BSA as standard.

SDS-PAGE Analysis and Immunoblotting

The purity of the protein preparations was estimated by SDS-PAGE using a Mini-Protean II electrophoresis cell (Bio-Rad) and silver (20) or Coomassie blue staining. The proteins separated by SDS-PAGE were electrophoretically transferred to a Immobilon-P membrane

(Millipore). After blocking, the membrane was probed for 2 h at room temperature with the primary antibody anti-NACE, obtained by immunization (16), diluted to 1:500. After washing, the immunoblot was incubated with the HRP-anti-mouse IgG (1:10,000) (Jackson ImmunoResearch) for 1h at room temperature. The blot was developed with a chemiluminescence kit (Amersham Biosciences).

Enzymatic Assays

*Sm*NACE catalytic activity was measured under saturating (400 μM) or limiting (10 μM) amounts of NAD^+ in the presence of 2.5×10^5 dpm [adenosine-U-^{14}C]NAD^+ (Amersham Biosciences) as described before (16). Briefly, the enzyme was suspended in Buffer A and incubated at 37°C with substrate (200 μL final volume). At selected times, aliquots (50 μL) were removed and enzyme activity was stopped by adding ice-cold perchloric acid (2% v/v final concentration). After neutralization with 3.5 M K_2CO_3, the precipitated proteins were removed by centrifugation. Product formation was monitored by HPLC on 300 x 3.9 mm μBondapack C_{18} (Waters) or 250 x 4.6 mm Acclaim C_{18} 5μm (Dionex) columns. The reaction products were eluted isocratically at a flow rate of 1 mL/min with a 10 mM ammonium phosphate buffer (pH 5.5) containing 0.8–1.2% (v/v) acetonitrile and detected by radiodetection (Flo-one, Packard Radiometric Instruments) when using [^{14}C]NAD^+ or by absorbance recording at 260nm. Kinetic parameters, K_m and V_{max}, were determined from the plots of the initial rates of product(s) (ADPR + cADPR) formation as a function of substrate concentration (5–400 μM NAD^+, 8 data points) according to Michaelis-Menten kinetics, using a nonlinear regression program (GraphPad, Prism).

The pH-dependent activities of WT *Sm*NACE and H103W mutant were determined using 1,N^6-etheno-NAD^+ (Sigma) as substrate. This continuous assay consists in measuring an increase (about 12-fold) of fluorescence (λ_{em} = 410 nm; λ_{exc} = 310 nm) resulting from the hydrolytic conversion of the dinucleotide to 1,N^6-etheno-ADPR (21). Reactions were performed at 37°C in 10 mM sodium citrate or potassium phosphate buffers at pH 4.0–8.0 (1 mL final volume) in a thermostatically controlled fluorimeter cuvette (Shimadzu, RF-5301). The kinetic parameters were calculated as above from the initial rates. The specificity constants V_{max}/K_m were determined alternatively from progress curves by using an initial 1,N^6-etheno-NAD^+ concentration of 2.0 μM. Under these conditions where $[S]_0 \ll K_m$, the values of V_{max}/K_m were directly obtained by fitting the curves to the equation: $[S] = [S]_0 exp(-K_m t/V_{max})$ (22,23). The apparent pKa values were calculated from plots of V_{max} and V_{max}/K_m as a function of pH (24) with a nonlinear curve-fitting program.

Methanolysis reactions catalyzed by *Sm*NACE were performed at 37°C in Buffer A in the presence of 50 μM NAD^+, [adenosine-U-^{14}C]NAD^+ (2.5×10^5 dpm) and 0–3 M methanol (200 μl final volume). Aliquots, taken at different time points, were treated as described above and the reaction products were analyzed by HPLC (25). The transformation of NGD^+ was followed fluorometrically (17). The assays were conducted, at 37°C, in Buffer A in the presence of 10–300 μM NGD^+ and enzyme in a 2 mL final volume. The fluorescence changes were monitored at λ_{em} = 410 nm (λ_{exc} = 310nm) corresponding to the appearance of cGDPR. The effect of 0–3 M methanol on cyclization rates of 100 μM NGD^+ was determined similarly and the relative proportions of the reaction products GDPR, cGDPR and *β*-methyl GDPR were determined by HPLC as described above; see also (7).

Inhibition Studies

Inhibition of the H103W mutant of *Sm*NACE by araF-NAD^+ was studied fluorometrically using 1,N^6-etheno-NAD^+ as substrate. Assays were performed in Buffer A in the presence of 60 μM 1,N^6-etheno-NAD^+ and 0–10 μM araF-NAD^+ (26) (final volume 1 mL). The reaction was started by addition of the enzyme and followed over time for 20 min. The progress curves

were analyzed as described previously (25,26) by fitting the slow-binding inhibition to the equation :

$$F=v_s t+(v_o - v_s)(1 - \exp(-kt))/k+F_0$$

Use of a nonlinear regression program yielded the different parameters, i.e. v_o, initial rate; v_s, steady-state rate; k, apparent first-order constant for reaching the steady-state enzyme-inhibitor complex; and F_0, the initial fluorescence. The kinetic parameters k_{off}, k_{on} and K_i (= k_{off}/k_{on}) were calculated from the plot of k against inhibitor concentration (6 data points) according to the equation:

$$k=k_{off}+k_{on}[I]/(1+[S]/K_m)$$

A $K_m = 23.8$ μM for $1,N^6$-etheno-NAD^+ (H103W mutant) was used for these calculations.

The same protocol was used to study the inhibition of the enzyme by Cibacron blue F3GA. In this case classical inhibition was observed and the IC_{50} value, i.e. the concentration of inhibitor that reduces the activity of the enzyme by 50%, was determined by nonlinear regression curve fitting.

Molecular Modeling of WT and H103W Mutant SmNACE

Five homology models of *Sm*NACE were generated using the Modeller 8.1 automodel protocol (27) with the crystallographic coordinates of human CD38 (1yh3), human CD157 (1isf) and *Aplysia* cyclase (1lbe) as templates. The N-terminal and C-terminal regions (1–11 and 285–303) were omitted in the model because of the lack of homologous template structures. The quality of the models was evaluated using Procheck and WHATIF (http://biotech.ebi.ac.uk). The best representative structure was optimized by energy minimization in implicit water using AMBER 8.0 (28) with the Parm99 parameter set and the Generalized-Born approach. The three-dimensional structure of the H103W mutant was obtained by the manual edition of WT *Sm*NACE in SYBYL 7.1. The rotameric state of the Trp^{103} residue was chosen based on the conformations of Trp^{101}, Trp^{109} and Trp^{125} observed in the crystal structures of *Aplysia* cyclase, human CD157/BST-1 and CD38, respectively. The region surrounding the mutation was relaxed by 1000 steps of Powell energy minimization in SYBYL 7.1 using Amber99 force field.

pKa Prediction of the Active Site Titratable Residues

Structures were prepared using PDB2PQR web server (29) and pKa calculations were performed by both PROPKA (http://propka.chem.uiowa.edu/) (30) and the Protein pKa Estimator (version 0.9, OpenEye Scientific Software, Inc.). The dielectric constant values used Poisson-Boltzmann equation (31) were set depending on the residue accessibility.

Conformational Analysis of cADPR and cGDPR

The crystal structure of free cADPR is published (32,33). cGDPR structure was obtained by manual edition of cADPR followed by a rapid energy minimization (default parameters) in SYBYL 7.1. Atom and bond types were set according to the known tautomeric states. The coordinates of both molecules were stored in MOL2 files. Conformational analysis were set up in Maestro ver. 7 (Schroedinger Inc.). For each compound, a 500-step Monte Carlo conformational search was performed in MacroModel ver. 8 (Schroedinger Inc.). An energy minimization in a simulated water environment was then performed on the compounds in their ionized state using the truncated-Newton conjugate-gradient method (TNCG) and AMBER* force field. Conformers were selected using a 3 kcal/mol energy cutoff and clustered based on RMS difference between corresponding torsion angles in pairs of structures using Xcluster (Schroedinger Inc.). Representative structures were analyzed using SYBYL 7.1.

Flexible Docking of NAD$^+$, NGD$^+$, cADPR and cGDPR into WT and Mutant SmNACE active sites

Protein and ligand input files were prepared using SYBYL 7.1. Atom typing, stereochemistry and local geometry were checked and all hydrogen atoms were added and coordinates were saved in MOL2 format. The docking simulations were carried out using GOLD ver. 3.0. (34). Binding site was defined using a sphere of 12 Å centered on the centroïd of the atom subset composed of His(Trp)[103] and Trp[165] side chains. The default parameters set was chosen to run the genetic algorithm. The Goldscore scoring function was used to evaluate poses. The automatic placement of the ligand was biaised by one to three intermolecular distance restraints (see Supporting Information). Docked poses were assessed using Silver 2.3.4.

RESULTS

Expression of the H103 Mutant of SmNACE

*Sm*NACE was subjected to site-directed mutagenesis to assess the functional significance of His[103]. In contrast to the wild-type recombinant enzyme (WT *Sm*NACE), which was produced in fairly good yield (16 mg/L) by the methylotrophic yeast *P. pastoris* (16), mutation of the single active site His[103] to Trp (H103W *Sm*NACE) resulted in a poorly expressed protein (~ 1 mg/L). Nevertheless, the expressed H103W mutant was secreted into the medium by *Pichia* and bound efficiently to a Cibacron blue affinity gel indicating a native-like conformation for its NAD$^+$ binding site (see below). After eluting the mutant H103W *Sm*NACE from the column of immobilized Cibacron blue, a second step purification on a Ni^{2+}-affinity gel was used to further purify the His-tagged protein. As found previously for the WT enzyme (16), the H103W *Sm*NACE was expressed by *Pichia* as two broad protein bands of approximately 41 and 43 kDa (Figure 3A). The molecular weight of the soluble recombinant protein is larger than the expected molecular mass (32 kDa) because NACE is heavily glycosylated (16). Identical to what we previously observed with WT *Sm*NACE (16), both protein bands from the yeast expressing H103W *Sm*NACE were recognized by polyclonal antibodies raised in response to immunization with the WT *Sm*NACE cDNA (Figure 3A).

The H103W Mutant of SmNACE has a Readily Measurable ADP-ribosyl Cyclase Activity

To determine the consequence of mutating the His[103] active site residue, the catalytic properties of the WT and H103W *Sm*NACE were compared. Replacing His[103] by a Trp residue had little impact on the specific activity of *Sm*NACE as the kinetic parameters (K_m and V_{max}) of the H103W mutant enzyme were very similar to that of the WT enzyme when NAD$^+$ was used as the substrate (Figure 3B and Table 1). As we previously reported (16, 35), when WT SmNACE was incubated in the presence of [^{14}C]NAD$^+$, the formation of cADPR could not be detected. In sharp contrast, the mutant H103W *Sm*NACE had clearly measurable ADP-ribosyl cyclase activity. As shown in Figure 3C, the cADPR peak was easily detected on HPLC profiles and it accounted for 6.8 ± 1.6 % ($n = 15$) of the reaction products (Table 2). In fact, compared to the activity of the WT *Sm*NACE enzyme, the replacement of His[103] with Trp[103] increased the ADP-ribosyl cyclase activity of *Sm*NACE by 2 to 3 orders of magnitude. This remarkable result points to the competence of the active site residue-103 in the partitioning of the E·ADP-ribosyl intermediate between cyclization and hydrolysis. The data further indicates that reintroduction of a Trp residue that is conserved in all other members of cyclase enzyme family to *Sm*NACE restores the ability of *Sm*NACE to catalyze the hallmark reaction of this class of enzymes, namely the ability to transform NAD$^+$ into cADPR. Comparatively, the H103W mutant of *Sm*NACE is even a better cyclase than CD38 and CD157.

Although WT *Sm*NACE is an extremely poor ADP-ribosyl cyclase, we previously showed that it is an excellent GDP-ribosyl cyclase and efficiently transformed the surrogate substrate NGD$^+$ into GDPR and cGDPR (16), with the cyclic compound accounting for approximately

85% of the reaction products (35). To determine whether the H103W mutant of *Sm*NACE was a more efficient GDP-ribosyl cyclase than the WT *Sm*NACE, we measured the kinetic parameters and the cyclization efficiency using using NGD^+ as a substrate. Similar to our results with NAD^+, the kinetic parameters for NGD^+ were directly comparable with the H103W mutant and WT *Sm*NACE (Table 1). Interestingly, the mutant was also a slightly better cyclase of NGD^+ as cGDPR accounted for 90.0 ± 1.3 % ($n = 5$) of the reaction products when H103W *Sm*NACE was incubated with NGD^+ (Table 1).

Methanolysis of NAD⁺ and NGD⁺ Catalyzed by the H103W SmNACE Mutant

We wanted to verify whether the mutation of *Sm*NACE altered the kinetic mechanism of the enzyme. First we confirmed that similar to WT *Sm*NACE (16) and other ADP-ribosyl cyclases such as CD38 (25,36,37), methanol acted as an alternate acceptor in the transformation of NAD^+ which competed with water to form, with complete retention of configuration, β-methyl ADPR at the expense of ADPR (Figure 1). Moreover, for a cyclase such as the H103W *Sm*NACE mutant, we predicted that the formation of cADPR as reaction product would also concomitantly decrease in the presence of methanol (8). This was borne out by experiment as the transformation of $[^{14}C]NAD^+$ in the presence of 3 M methanol yielded ADPR and β-methyl ADPR (2/3 and 1/3 of the reaction products, respectively) while cADPR was barely measurable (< 1% of reaction products)(Figure 3D). The partition ratio K (= [β-methyl ADPR]/[ADPR] x $[H_2O]/[CH_3OH]$), which indicates the relative reactivity of the E.ADP-ribosyl intermediate with water and methanol, was calculated to be 9.5 ± 1.5 ($n = 12$) which is somewhat higher than 5.0, the value found for WT *Sm*NACE (16). Next, we checked whether methanol (0–3 M) had any effect on the turnover rate of the catalyzed reaction. In the presence of 3 M methanol, i.e. the highest concentration used which results in the formation of the methanolysis product in a 34 % proportion of reaction products, we could not measure an increased transformation rate of NAD^+. A similar absence of acceleration was previously observed with the WT enzyme (16), indicating that the formation of the reaction intermediate is the rate limiting step in both WT and H103W *Sm*NACE. Altogether these results indicate that H103W mutation does not drastically affect the selectivity of the reaction intermediate vs. acceptors in the solvolytic step and nor does it affect the rate limiting step of the reaction catalyzed by *Sm*NACE.

We also studied the effect of methanol on the transformation of NGD^+. As described above, this dinucleotide is overwhelmingly converted into cGDPR by WT *Sm*NACE and the hydrolytic pathway yielding GDPR is not favored. However, as assessed by the fluorometric monitoring of the transformation of NGD^+ into cGDPR catalyzed by the WT *Sm*NACE, addition of methanol resulted in a marked inhibition of the cyclization rate (up to 23% in the presence of 3 M methanol) (Figure 4A). HPLC analysis of the reaction products revealed that this inhibition was accompanied, as expected, by a concomitant decreased formation of cGDPR and by the appearance of the methanolysis product β-methyl GDPR (not shown). This result is consistent with the occurrence of a methanolysis reaction at the expense of the cyclization reaction and with a preferential reactivity of the E.GDP-ribosyl intermediate with methanol compared to water. For example at 3 M methanol, the production of cGDPR by WT *Sm*NACE was reduced to 60% of reaction products, whereas β-methyl GDPR accounted for 23%. The solvolysis/cyclization ratio (i.e. [GDPR+β-methyl GDPR]/[cGDPR]) was linearly correlated with the concentration of methanol (Figure 4B) – excluding a preferential binding of this solvent to the active site within this concentration range – and the partition ratio K was about 30 ± 4 ($n = 6$). Interestingly, methanol had a much lesser effect on the reaction catalyzed by the H103W *Sm*NACE mutant (Figure 4A); this was borne out by HLPC analysis which showed that even at 3 M methanol, β-methyl GDPR accounted only for about 3 % of the reaction products. These results indicate that H103W mutation which results in an increased NGD^+ cyclization efficiency, concomitantly also renders the solvolytic alternate pathway less competitive. The occurrence of such an inverse correlation is highly reminiscent of the results

we have obtained previously with *A. californica* ADP-ribosyl cyclase. During the catalytic transformation of NGD^+, this enzyme kinetically favors the cyclization of the GDP-ribosyl intermediate to such an extent that intermolecular reactions with water or methanol cannot compete with the intramolecular pathway (7).

Comparison of the Inhibition of WT and H103W Mutant of SmNACE by AraF-NAD⁺ and Cibacron Blue F3GA

A very interesting feature of *Sm*NACE is that this enzyme is much less sensitive to inhibition by molecules such as araF-NAD^+ and Cibacron blue F3GA. This observation suggests that the differences within the active site of *Sm*NACE might be exploited to design inhibitors that are specific for the schistosome enzymes. AraF-NAD^+ is one of the most potent inhibitors (nM range) known for CD38 and it belongs to the class of slow-binding inhibitors (25,26). In contrast, this molecule was found to be only a very modest inhibitor ($IC_{50} \gg 10 \mu M$) of *Sm*NACE (16). To test whether the residue at position 103 might play a crucial role in the mode of interaction of inhibitors to the active site of *Sm*NACE, we studied the inhibition of the H103W mutant by these two molecules.

In the presence of araF-NAD^+ progress curves typical of a slow-binding inhibition could be observed (not shown). Under our experimental conditions the initial rates v_0 (see Experimental Procedures) were not affected by this NAD^+ analogue, which is indicative of a slow interconversion between E and E.I, the enzyme.inhibitor complex (38). The following constants were calculated for the formation of E.I: $k_{on} = 1.88 \times 10^3 M^{-1}s^{-1}$, $k_{off} = 1.5 \times 10^{-3} s^{-1}$ ($t_{1/2} = 7.7$ min) and $Ki = 0.80 \mu M$. Thus, the presence of Trp^{103} seems to be instrumental in the binding affinity of araF-NAD^+ which is at least 2 orders of magnitude higher than for the WT NACE active site.

Cibacron blue F3GA is a water soluble triazine dye which has been used as inhibitor of enzymes binding mononucleotides such as ATP (39) or dinucleotides such as $NAD(P)^+$. The high affinity of Cibacron blue for the active site of this large variety of enzymes results from a complex combination of hydrophobic, electrostatic and hydrogen bonding interactions. Some structural studies have however revealed that the dye is primarily a mimic for the ADP moiety of the mono(di)nucleotides (40,41). The immobilized form of the blue dye on solid supports has been widely exploited for protein purification by pseudo-affinity chromatography (42, 43), and has been used to purify cyclase family members, including CD38 (44) and *Sm*NACE (16). In addition, Cibracon blue F3GA is a potent inhibitor of CD38 enzyme activity with an $IC_{50} = 17.8 \pm 4.4$ nM and $0.190 \pm 0.027 \mu M$ for recombinant bovine or human CD38, respectively (H. Muller-Steffner, unpublished). However, this dye is a less potent inhibitor of WT *Sm*NACE for which a $IC_{50} = 1.15 \pm 0.14 \mu M$ was measured (Figure 4C). Interestingly, the H103W mutation increases the inhibitory power of Cibacron blue about 5-fold with a $IC_{50} = 0.23 \pm 0.05 \mu M$ (Figure 4C). This effect – although modest – suggests that residue-103 within the active site of *Sm*NACE could be part of the Cibacron blue binding pocket and that the bulkier hydrophobic side chain of the Trp^{103} residue of the mutant is somewhat better able to provide nonpolar interactions with the aromatic rings of the dye than the WT His^{103} residue.

Modeling of the WT SmNACE and H103W Mutant Active Sites

To determine the impact on catalysis of the interactions between His^{103} and other critical residues, we modeled the active sites of WT and H103W mutant of *Sm*NACE. The side chains of Glu^{124} and Glu^{202}, which are two active site residues crucial for catalytic activity of *Sm*NACE, are in close vicinity to the imidazole ring of His^{103} in the WT enzyme (Figure 5A). In the three-dimensional model, the distances measured between the carboxylate and imidazole groups are about 4.0 and 6.7 Å for Glu^{124} and Glu^{202}, respectively. The replacement of the titratable His^{103} by a non-ionizable tryptophan results in significant modifications of the

electrostatic environment of the two Glu (Figure 5B). Accordingly, we have predicted the pKa values of the Glu[124] and Glu[202] carboxylic groups using an empirical method and a method based on an electrostatic continuum models that numerically solves the linearized Poisson-Boltzmann equation. Although each approach yields somewhat different absolute values (Table 2), they both support the propensity of the two Glu residues to *become less acidic* upon replacement of His[103] with a tryptophan. The most dramatic pKa shift is observed in the mutant for Glu[124] (ΔpKa = + 1.45 to + 4.25). For comparison, pKa values observed in the H103W mutant are quite similar to those predicted for the equivalent residues in human CD38. Importantly, it should be stressed that Glu[124] and Glu[202] are the only titratable residues within the active site whose pKa's can be affected by the H103W mutation.

The values of these ionizable groups can also be approached experimentally by studying the dependence of the kinetic parameters of WT and H103W *Sm*NACE on pH. The pH-activity profiles were determined using the substrate 1,N[6]-etheno-NAD^{+} and, in the range between 5.0 to 8.0, the plot of the values of V_{max} *versus* pH for the wild-type enzyme reveals a single critical ionizable residue with a pKa value of 5.82 ± 0.07 (Figure 4D). In this pH range the K_m values remained essentially constant and the pH profile of V_{max}/K_m *vs.* pH yielded a similar pKa of 6.05 ± 0.10 (Figure 4E). This residue, which must be unprotonated for activity, has an ionization constant consistent with the pKa expected for a histidine side-chain in a relatively non-polar environment. Interestingly, the experimental values obtained here are close to the pKa predicted for His[103] using the electrostatic continuum model (Table 2). In the absence of His[103], a more acidic group with a pKa value of 5.4 ± 0.1 was similarly found in the H103W mutant by studying the effect of the 4.0–7.5 pH range on the values of V_{max}/K_m (Figure 4E). The identity of this residue which is critical for the activity of the mutant is unknown; however catalytic Glu[202] which is less acidic than Glu[124] and whose pKa is somewhat shifted upwards in the H103W mutant (Table 2) could be an excellent candidate.

To assess the substrate binding mode, NAD^{+} was successfully docked into the active site of *Sm*NACE using the program GOLD 3.0. The best poses obtained for WT and H103W mutant *Sm*NACE are very similar (Figure 5C,D). The nicotinamide ring is buried within the active site pocket in an essentially apolar environment, making it likely to engage in a strong π-stacking interaction with Trp[165] and to establish an edge-to-face aromatic interaction with His/Trp[103]. Interestingly, according to this model a neutral form of the imidazole ring of His[103], as well as the 5-membered pyrrole ring part of Trp[103], are also in favorable position for carbohydrate-aromatic interactions (45) involving the cluster of the C-H bonds on the β-face of the ribose linked to nicotinamide. A similar ribose-aromatic interaction has been observed recently in a crystal structure of *A. californica* ADP-ribosyl cyclase with a covalently bound ribose-5′-phosphate (46). The adenine moiety of NAD^{+} is positioned outside this cleft in an *anti* conformation with the base away from the ribose ring. In this conformation the distance between adenine N1 and nicotinamide-attached ribose C1″ is approximately 10 Å. Consequently, the formation of cADPR implies a rotation from this *anti* to a *syn* conformation of the adenine with respect to the N9-ribose bond.

Next, to provide a better understanding of the structural determinants which govern the cyclase *vs.* hydrolase reaction selectivity observed for NAD^{+} and NGD[+], we first compared the three dimensional structures of cADPR and cGDPR. Conformational space explored by cADPR and cGDPR was sampled using the MacroModel program (Figure S1 in Supporting Information). The cADPR conformational search reproduced the available crystal structure of free cADPR (32, 33), thereby validating the efficiency of the method to predict reliable three-dimensional structures. Indeed, the adenine moiety of cADPR was found in *syn* conformation about the N9-C1′ ribose bond and in *anti* conformation about the N1-C1″ ribose bond. The exploration of cGDPR structure indicated that the guanine base is in *anti* conformation about the N9-C1′ ribose bond. Both *syn* and *anti* orientations were observed with respect to the N7-C1″-ribose

of cGDPR. The superimposition of the ribose and pyrophosphate heavy atoms of cADPR and cGDPR (Figure 6A) results in a minimal base overlap and quite distinct distributions of donor and acceptor H-bonds. Moreover, the guanine ring contains more polar residues than adenine and is less aromatic. Together, all these features suggest different binding modes for adenine and guanine moieties during the cyclization reaction.

If we make the reasonable assumption that reactions catalyzed by *Sm*NACE occur according to molecular mechanisms similar to those advocated for the other ADP-ribosyl cyclases (3), the ribosyl moiety of the A(G)DP-ribosyl intermediate generated by the nicotinamide-ribose bond cleavage would be expected to be close to the carboxylate of Glu[202]. Based on this premise, we generated theoretical three-dimensional models of complexes between cADPR or cGDPR and WT or mutant *Sm*NACE. As expected, different base positioning were observed for cADPR and cGDPR (Figure 6B,C). The binding of adenine into the *Sm*NACE active site cleft may be principally mediated by π-stacking and Van der Waals interactions with His/Trp[103] and Trp[165] residues. These interactions are significantly favored in the H103W mutant. By contrast, guanine may preferentially interact with the active site using H-bonds and consequently, the H103W mutation is not predicted to have a dramatic effect on guanine binding.

DISCUSSION

In this study we demonstrated that replacement of His[103] in the active site of *S. mansoni* NACE by a tryptophan – a residue conserved in all the other members of the ADP-ribosyl cyclase family – results in a dramatic increase (2 to 3 orders of magnitude) in the ADP-ribosyl cyclase activity of this enzyme. Thus, in contrast to the WT *Sm*NACE, the transformation of NAD^{+} catalyzed by the H103W mutant yields a readily detectable proportion of cADPR which amounts to about 7% of the reaction products. Importantly, replacement of His[103] with a tryptophan has no consequence on the kinetic parameters of *Sm*NACE (Table 1) indicating that the increased efficiency of the cyclization step observed in the H103W mutant does not originate from changes in the ground-state binding of the substrate or from an overall change of the transition state energy of the catalyzed reaction. For H103W *Sm*NACE, these data are consistent with a partitioning kinetic mechanism (Figure 1A) in which : *i*) the formation of the E·ADP-ribosyl intermediate is a rate-limiting step, as found for the WT *Sm*NACE (16) and mammalian CD38 (3), and *ii*) the increased rate of the intramolecular reaction of the ADP-ribosyl intermediate, leading to cADPR, occurs at the expense of its reaction with water. In further support of this mechanism, trapping experiments with methanol which acts as a powerful nucleophilic acceptor in competition with water and the intramolecular cyclization process in the transformation of the common E·ADP-ribosyl intermediate, show that the catalyzed reaction turnover in not accelerated. Altogether, the key observation made in this study is that the introduction of tryptophan residue at position 103 of the active site unmasks an alternate pathway which diverts the ADP-ribosyl intermediate towards the intramolecular cyclization process.

Surprisingly, despite the importance of Trp[103] in the *Sm*NACE mutant, no role for the equivalent active site residue Trp[125] in controlling the ADP-ribosyl cyclase activity was described in human CD38 (13). However, previous studies from our laboratory (15) and from the Lee laboratory (14) showed that the Glu residue in the 'signature region' (Glu[150] and Glu[146] in respectively mouse and human CD38) dictated whether cyclization or hydrolysis of NAD^{+} was the favored reaction pathway. Thus mutation of this active site residue resulted in a significant increase in the transformation of NAD^{+} into cADPR by murine CD38 which accounted for up to 25% of the reaction products (15). Likewise for the E146A mutant of human CD38, cADPR amounted to about 75 % of the total reaction products (14). However, unlike what we observed with the H103W mutant of *Sm*NACE, mutation of the 'signature' Glu residue

increased the cyclization at the expense of the reaction turnover which was reduced by more than 95% (15,47). Interestingly, replacement of Glu[146] in human CD38 by residues with small and neutral side chains favored the cyclization process, which has been suggested to be correlated with a reduced access of water molecules to the enzyme active site (14). Therefore, it appears that mutation of the active site 'signature' Glu residue, which seemingly controls the partitioning of the reaction intermediate in CD38, also affects the overall efficacy of its catalytic process. If the 'signature' Glu is responsible for controlling the partitioning of the reaction intermediate in CD38, why would mutation of His[103] to a Trp alter the cyclization efficiency of *Sm*NACE ? As we showed in Table 2, the 'signature' Glu[124] in H103W *Sm*NACE has an estimated pKa close to that of Glu[146], its equivalent residue in human CD38, and both values are much higher than the calculated pKa of Glu[124] in WT *Sm*NACE. We believe that the increased polarity of the highly acidic carboxylic group of Glu[124] in the WT *Sm*NACE may explain, at least in part, the reaction specificity of *Sm*NACE which, by increasing the solvation of the active site, might provide a more efficient activation of the water molecule involved in the nucleophilic attack of the reaction intermediate thus favoring the hydrolysis pathway. In support of this conclusion, our modeling studies indicated that the presence of His[103] appears to increase the polarity within a specific sub-domain of the active site, in the vicinity of the 'signature residue' Glu[124]. This would promote greater access of water molecules to the active site, favoring the hydrolytic pathway leading to ADPR at the expense of the cyclization reaction and cADPR production.

Although the active site of *S. mansoni* NACE and *S. japonicum* NACE contain a His instead of the Trp residue that is found in all other ADP-ribosyl cyclase family members (Figure 2), this change does not affect the overall catalytic activity of the enzyme but only influences the cyclase efficiency of the enzyme. This leads to the question of why WT *Sm*NACE is as efficient as the other ADP-ribosyl cyclases in the catalytic cleavage of the nicotinamide-ribose bond of NAD$^+$ which is the most energy-demanding step of the kinetic mechanism of these enzymes. Our modeling studies indicate that the active site Trp[103], found in all other CD38 family members and in H103W *Sm*NACE, partners with the other Trp found in the active site (Trp[165] in *Sm*NACE), to efficiently engage in stacking interactions (most probably edge-to-face type) with the nicotinamide moiety of the substrate. This stacking interaction can be mimicked by a neutral His[103] residue found in WT *Sm*NACE (Figure 7). Such an aromatic/hydrophobic environment – which also includes Leu[123] of the signature region – and the absence of solvent in the vicinity of the positively charged pyridinium moiety in NAD$^+$ was previously shown to significantly lower the barrier of dissociation of the nicotinamide-ribose bond (48-50). Moreover, our docking experiments predict that uncharged His[103] and Trp[103], via its 5-membered pyrrole ring, are both placed above the reacting ribose and thus could also stabilize – via σ-donor (His[103]) (51) or cation-π (Trp[103]) (52,53) type interactions – the oxocarbenium ion-like transition state occurring en route to the ADP-ribosyl reaction intermediate (Figure 1B) (3) and, as above, promote the cleavage of the scissile bond (Figure 7). Therefore we can infer that a *neutral imidazole* side-chain is needed for catalysis and that protonation of His[103] should result in a drastic decrease of activity in *Sm*NACE. In agreement with this hypothesis, we have found experimentally in the WT enzyme a group that titrates with a pKa of ~ 6.0 (Figure 4), i.e. a value close to the one predicted for His[103] (Table 2). This group was not detected in the H103W mutant but interestingly another ionizable group important for catalysis with a pKa of 5.4 was found. We have tentatively attributed this group to Glu[202], the catalytic residue essential for activity in the ADP-ribosyl cyclase enzyme family (9,13,54). According to the prevalent reaction mechanism for this family of enzymes (3) and in analogy with reactions catalyzed by glycosidases (55) this acid residue, when ionized, is involved in the stabilization of the transition state and of the reaction intermediate (Figure 1B). As discussed earlier, because of the presence of His[103], the residue Glu[202] is more acidic in the WT *Sm*NACE (Table 2) than in the H103W mutant and thus could not be detected within the pH range investigated where the active site His[103] titrates first.

We previously showed that in dramatic contrast with NAD^+, the cyclization reaction pathway is favored in the catalytic transformation of the alternate substrate NGD^+ by *Sm*NACE (16). As shown here, the H103W mutation does not significantly alter this reaction which overwhelmingly yields the cyclized reaction product, cGDPR. This suggests that the interaction of NAD^+ and NGD^+, and their cyclic derivatives cADPR and cGDPR, with the active site of *Sm*NACE is different enough to affect the outcome of the catalytic reaction. Docking of cADPR in the active site to model the ADP-ribosyl intermediate poised for the intramolecular cyclization reaction (Figure 1B), suggests that the *Sm*NACE residue 103 directly interacts with the adenine moiety of NAD^+ (Figure 6B). In contrast, this residue does not seem to be a key determinant for the positioning of the guanine moiety in cGDPR, in either the WT or H103W mutant *Sm*NACE (Figure 6C). To explain the NAD^+ cyclization vs. hydrolysis selectivity by *Sm*NACE, we suggest that replacement of His^{103} by a Trp residue might allow a better π-stacking of the adenine ring in the H103W mutant (Figure 6B), providing an orientation within the ADP-ribosyl intermediate that favors the intramolecular cyclization reaction between adenine-N1 and ribose-C1″. The absence of such interactions in the transformation of NGD^+ is consistent with our experimental results indicating only minor changes in the proportions of cyclic and solvolytic products upon H103W mutation (for a comparison with known adenine and guanine binding sites in proteins, see Supporting Information).

In conclusion, it is of interest to understand why the active site of *S. mansoni* NACE contains a His residue at position 103 instead of the tryptophan residue that is found in all other ADP-ribosyl cyclase family members. We suggest that *Sm*NACE has evolved to be an efficient NAD^+glycohydrolase and a very poor ADP-ribosyl cyclase. This implies two separate conditions: *i*) that the first step of the reaction mechanism, which generates an ADP-ribosyl intermediate from NAD^+ (Figure 1), is – as demonstrated in this work – equally efficient for the enzymes of the ADP-ribosyl cyclase family regardless of whether the active site residue at position 103 in *Sm*NACE (or the analogous position in CD38 or *Aplysia* cyclase) is a Trp or a His, and *ii*) that the specificity of these enzymes in terms of hydrolysis vs. cyclization must depend on the outcome of competing reaction pathways during the second part of the kinetic mechanism. Why this particular "mutation" was selected for during the evolution of the schistosomes is unknown. However, the fact that *S. mansoni* NACE, which is a GPI-anchored ecto-enzyme preferentially expressed at the surface (tegument) of adult worms (16), is lacking the "hallmark" enzyme activity of all other cyclases, suggests that there might be some functional advantage to the parasite to express this "defective" form of the enzyme. Regardless, the data presented here clearly demonstrate that *Sm*NACE can be converted from an enzyme that only generates ADPR into one that can produce both cADPR and ADPR by simply changing the active site His^{103} "back" to the canonical tryptophan. In this respect residue-103 which shifts the product selectivity in *Sm*NACE without affecting its catalytic activity fulfills the criteria of a "plasticity residue" in a promiscuous (or multifunctional) enzyme (56).

Supplementary Material

Refer to Web version on PubMed Central for supplementary material.
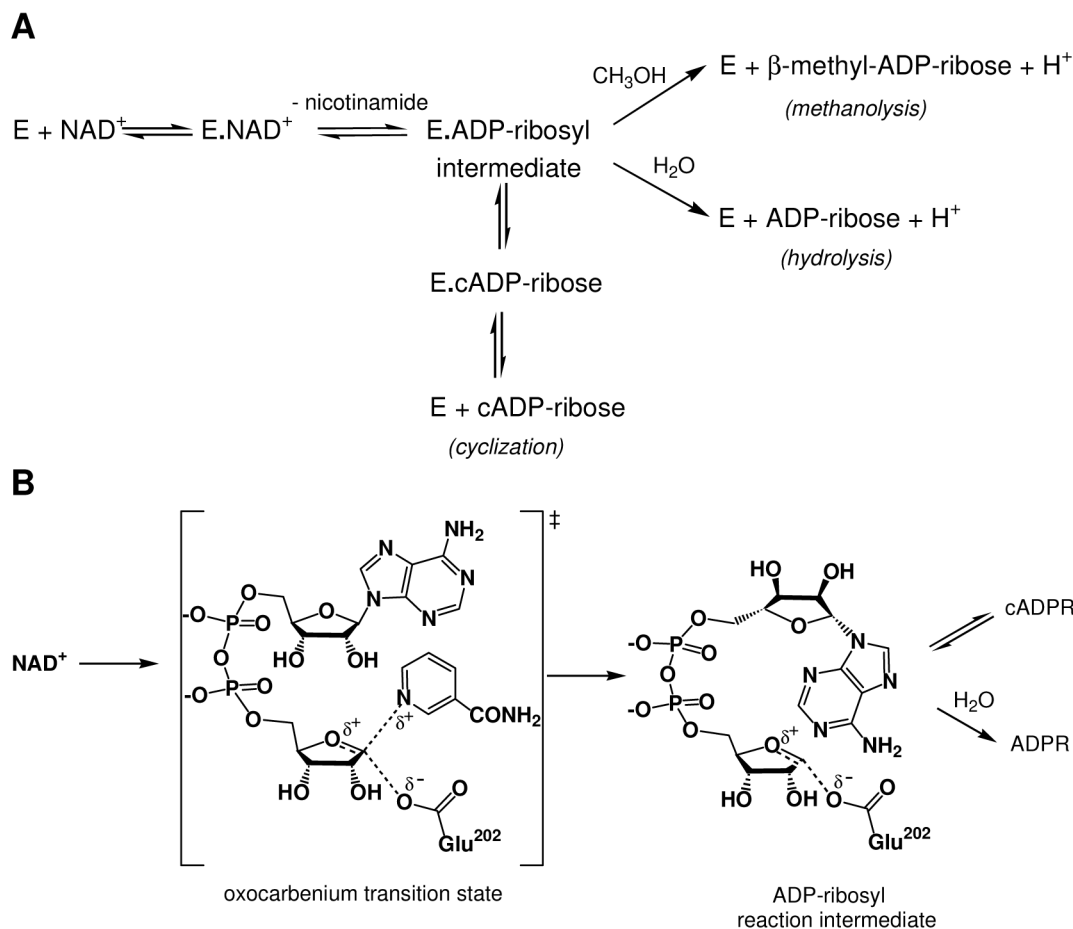
Acknowledgements

References

1. Howard M, Grimaldi JC, Bazan JF, Lund FE, Santos-Argumedo L, Parkhouse RM, Walseth TF, Lee HC. Formation and hydrolysis of cyclic ADP-ribose catalyzed by lymphocyte antigen CD38. Science 1993;262:1056–1059. [PubMed: 8235624]

2. Lee HC. Enzymatic functions and structures of CD38 and homologs. Chem Immunol 2000;75:39–59. [PubMed: 10851778]

3. Schuber F, Lund FE. Structure and enzymology of ADP-ribosyl cyclases: Conserved enzymes that produce multiple calcium mobilizing metabolites. Curr Mol Med 2004;4:249–261. [PubMed: 15101683]

4. Lee HC. Nicotinic acid adenine dinucleotide phosphate (NAADP)-mediated calcium signaling. J Biol Chem 2005;280:33693–33696. [PubMed: 16076847]

5. Hirata Y, Kimura N, Sato K, Ohsugi Y, Takasawa S, Okamoto H, Ishikawa J, Kaisho T, Ishihara K, Hirano T. ADP ribosyl cyclase activity of a novel bone marrow stromal cell surface molecule, BST-1. FEBS Lett 1994;356:244–248. [PubMed: 7805847]

6. Lee HC, Aarhus R. ADP-ribosyl cyclase: an enzyme that cyclizes NAD^+ into a calcium-mobilizing metabolite. Cell Regul 1991;2:203–209. [PubMed: 1830494]

7. Cakir-Kiefer C, Muller-Steffner H, Schuber F. Unifying mechanism for Aplysia ADP-ribosyl cyclase and CD38/NAD^+glycohydrolases. Biochem J 2000;349:203–210. [PubMed: 10861229]

8. Muller-Steffner HM, Augustin A, Schuber F. Mechanism of cyclization of pyridine nucleotides by bovine spleen NAD^+glycohydrolase. J Biol Chem 1996;271:23967–23972. [PubMed: 8798630]

9. Sauve AA, Deng HT, Angeletti RH, Schramm VL. A covalent intermediate in CD38 is responsible for ADP-ribosylation and cyclization reactions. J Am Chem Soc 2000;122:7855–7859.

10. Prasad GS, McRee DE, Stura EA, Levitt DG, Lee HC, Stout CD. Crystal structure of Aplysia ADP ribosyl cyclase, a homologue of the bifunctional ectozyme CD38. Nature Struct Biol 1996;3:957–964. [PubMed: 8901875]

11. Yamamoto-Katayama S, Ariyoshi M, Ishihara K, Hirano T, Jingami H, Morikawa K. Crystallographic studies on human BST-1/CD157 with ADP- ribosyl cyclase and NAD glycohydrolase activities. J Mol Biol 2002;316:711–723. [PubMed: 11866528]

12. Liu Q, Kriksunov IA, Graeff R, Munshi C, Lee HC, Hao Q. Crystal structure of human CD38 extracellular domain. Structure 2005;13:1331–1339. [PubMed: 16154090]

13. Munshi C, Aarhus R, Graeff R, Walseth TF, Levitt D, Lee HC. Identification of the enzymatic active site of CD38 by site-directed mutagenesis. J Biol Chem 2000;275:21566–21571. [PubMed: 10781610]

14. Graeff R, Munshi C, Aarhus R, Johns M, Lee HC. A single residue at the active site of CD38 determines its NAD cyclizing and hydrolyzing activities. J Biol Chem 2001;276:12169–12173. [PubMed: 11278881]

15. Lund FE, Muller-Steffner HM, Yu N, Stout CD, Schuber F, Howard MC. CD38 signaling in B lymphocytes is controlled by its ectodomain but occurs independently of enzymatically generated ADP-Ribose or cyclic ADP-Ribose. J Immunol 1999;162:2693–2702. [PubMed: 10072513]

16. Goodrich SP, Muller-Steffner H, Osman A, Moutin M-J, Kusser K, Roberts A, Woodland DL, Randall TD, Kellenberger E, LoVerde PT, Schuber F, Lund FE. Production of calcium-mobilizing metabolites by a novel member of the ADP-ribosyl cyclase family expressed in *Schistosoma mansoni*. Biochemistry 2005;44:11082–11097. [PubMed: 16101292]

17. Graeff RM, Walseth TF, Fryxell K, Branton WD, Lee HC. Enzymatic synthesis and characterizations of cyclic GDP-ribose. A procedure for distinguishing enzymes with ADP-ribosyl cyclase activity. J Biol Chem 1994;269:30260–30267. [PubMed: 7982936]

18. Hu W, Yan Q, Shen DK, Liu F, Zhu ZD, Song HD, Xu XR, Wang ZJ, Rong YP, Zeng LC, Wu J, Zhang X, Wang JJ, Xu XN, Wang SY, Fu G, Zhang XL, Wang ZQ, Brindley PJ, McManus DP, Xue CL, Feng Z, Chen Z, Han ZG. Evolutionary and biomedical implications of a Schistosoma japonicum complementary DNA resource. Nat Genet 2003;35:139–147. [PubMed: 12973349]

19. Clare JJ, Romanos MA, Rayment FB, Rowedder JE, Smith MA, Payne MM, Sreekrishna K, Henwood CA. Production of mouse epidermal growth factor in yeast: high-level secretion using Pichia pastoris strains containing multiple gene copies. Gene 1991;105:205–212. [PubMed: 1937016]

20. Morrissey JH. Silver stain for proteins in polyacrylamide gels: a modified procedure with enhanced uniform sensitivity. Anal Biochem 1981;117:307–310. [PubMed: 6172996]

21. Muller CD, Tarnus C, Schuber F. Preparation of analogues of NAD^+ as substrates for a sensitive fluorimetric assay of nucleotide pyrophosphatase. Biochem J 1984;223:715–721. [PubMed: 6150704]

22. Orsi BA, Tipton KF. Kinetic analysis of progress curves. Methods Enzymol 1979;63:159–183. [PubMed: 502859]

23. Meyer-Almes FJ, Auer M. Enzyme inhibition assays using fluorescence correlation spectroscopy: A new algorithm for the derivation of k(cat)/K(M) and K(i) values at substrate concentrations much lower than the Michaelis constant. Biochemistry 2000;39:13261–13268. [PubMed: 11052679]

24. Tipton AK, Dixon HBF. Effect of pH on enzymes. Methods Enzymol 1979;63:183–234. [PubMed: 41155]

25. Berthelier V, Tixier JM, Muller-Steffner H, Schuber F, Deterre P. Human CD38 is an authentic NAD (P)$^+$ glycohydrolase. Biochem J 1998;330:1383–1390. [PubMed: 9494110]

26. Muller-Steffner HM, Malver O, Hosie L, Oppenheimer NJ, Schuber F. Slow-binding inhibition of NAD$^+$glycohydrolase by arabino analogues of beta-NAD$^+$ J Biol Chem 1992;267:9606–9611. [PubMed: 1315761]

27. Sali A, Blundell TL. Comparative protein modelling by satisfaction of spatial restraints. J Mol Biol 1993;234:779–815. [PubMed: 8254673]

28. Case DA, Cheatham TE 3rd, Darden T, Gohlke H, Luo R, Merz KM Jr, Onufriev A, Simmerling C, Wang B, Woods RJ. The Amber biomolecular simulation programs. J Comput Chem 2005;26:1668–1688. [PubMed: 16200636]

29. Dolinsky TJ, Nielsen JE, McCammon JA, Baker NA. PDB2PQR: an automated pipeline for the setup of Poisson-Boltzmann electrostatics calculations. Nucleic Acids Res 2004;32:W665–667. [PubMed: 15215472]

30. Yang AS, Gunner MR, Sampogna R, Sharp K, Honig B. On the calculation of pKas in proteins. Proteins 1993;15:252–265. [PubMed: 7681210]

31. Bashford D, Karplus M. pKa's of ionizable groups in proteins: atomic detail from a continuum electrostatic model. Biochemistry 1990;29:10219–10225. [PubMed: 2271649]

32. Lee HC, Aarhus R, Levitt D. The crystal structure of cyclic ADP-ribose [letter]. Nature Struct Biol 1994;1:143–144. [PubMed: 7656029]

33. Lee, HC. Cyclic ADP-ribose and NAADP. In: Lee, HC., editor. Cyclic ADP-ribose and NAADP Structures, metabolism and functions. Kluwer Academic Publishers; Boston: 2002. p. 1-21.

34. Verdonk ML, Cole JC, Hartshorn MJ, Murray CW, Taylor RD. Improved protein-ligand docking using GOLD. Proteins 2003;52:609–623. [PubMed: 12910460]

35. Lund FE, Moutin MJ, Muller-Steffner H, Schuber F. ADP-ribosyl cyclase and GDP-ribosyl cyclase activities are not always equivalent: Impact on the study of the physiological role of cyclic ADP-ribose. Anal Biochem 2005;346:336–338. [PubMed: 16212930]

36. Muller-Steffner H, Muzard M, Oppenheimer N, Schuber F. Mechanistic implications of cyclic ADP-ribose hydrolysis and methanolysis catalyzed by calf spleen NAD$^+$glycohydrolase. Biochem Biophys Res Commun 1994;204:1279–1285. [PubMed: 7980606]

37. Sauve AA, Munshi C, Lee HC, Schramm VL. The reaction mechanism for CD38. A single intermediate is responsible for cyclization, hydrolysis, and base-exchange chemistries. Biochemistry 1998;37:13239–13249. [PubMed: 9748331]

38. Morrison JF, Walsh CT. The behavior and significance of slow-binding enzyme inhibitors. Adv Enzymol Relat Areas Mol Biol 1988;61:201–301. [PubMed: 3281418]

39. Thompson ST, Stellwagen E. Binding of Cibacron blue F3GA to proteins containing the dinucleotide fold. Proc Natl Acad Sci USA 1976;73:361–365. [PubMed: 174104]

40. Biellmann JF, Samama JP, Brändén CI, Eklund H. X-ray studies of the binding of Cibacron blue F3GA to liver alcohol dehydrogenase. Eur J Biochem 1979;102:107–110. [PubMed: 520314]

41. Prestera T, Prochaska HJ, Talalay P. Inhibition of NAD(P)H:(quinone-acceptor) oxidoreductase by cibacron blue and related anthraquinone dyes: a structure-activity study. Biochemistry 1992;31:824–833. [PubMed: 1731940]

42. Thompson ST, Cass KH, Stellwagen E. Blue dextran-sepharose: an affinity column for the dinucleotide fold in proteins. Proc Natl Acad Sci USA 1975;72:669–672. [PubMed: 164664]

43. Denizli A, Piskin E. Dye-ligand affinity systems. J Biochem Biophys Meth 2001;49:391–416. [PubMed: 11694290]

44. Schuber F, Pascal M. Interaction of Blue Dextran and Cibacron Blue F3GA with calf spleen NAD^+-glycohydrolase. Biochimie 1977;59:735–737. [PubMed: 202341]

45. del Carmen Fernandez-Alonso M, Canada FJ, Jimenez-Barbero J, Cuevas G. Molecular recognition of saccharides by proteins. Insights on the origin of the carbohydrate-aromatic interactions. J Am Chem Soc 2005;127:7379–7386. [PubMed: 15898786]

46. Love ML, Szebenyi DME, Kriksunov IA, Thiel DJ, Munshi C, Graeff R, Lee HC, Hao Q. ADP-ribosyl cyclase: Crystal structures reveal a covalent intermediate. Structure 2004;12:477–486. [PubMed: 15016363]

47. Lund FE, Muller-Steffner H, Romero-Ramirez H, Moreno-Garcia ME, Partida-Sanchez S, Makris M, Oppenheimer NJ, Santos-Argumedo L, Schuber F. CD38 induces apoptosis of a murine pro-B leukemic cell line by a tyrosine kinase-dependent but ADP-ribosyl cyclase- and NAD glycohydrolase-independent mechanism. Int Immunol 2006;18:1029–1042. [PubMed: 16720618]

48. Oppenheimer NJ. NAD hydrolysis: Chemical and enzymatic mechanisms. Mol Cell Biochem 1994;138:245–251. [PubMed: 7898470]

49. Buckley N, Handlon AL, Maltby D, Burlingame AL, Oppenheimer NJ. Reactions of charged substrates. 2 Gas-phase dissociation of 2′-substituted nicotinamide arabinosides. J Org Chem 1994;59:3609–3615.

50. Buckley N, Oppenheimer NJ. Reactions of Charged Substrates. 5 The Solvolysis and Sodium Azide Substitution Reactions of Benzylpyridinium Ions in Deuterium Oxide. J Org Chem 1996;61:7360–7372. [PubMed: 11667662]

51. Hu J, Barbour LJ, Ferdani R, Gokel GW. Sodium cation complexation behavior of the heteroaromatic sidechains of histidine and tryptophan. Chem Commun (Camb) 2002:1810–1811. [PubMed: 12271620]

52. Zacharias N, Dougherty DA. Cation-pi interactions in ligand recognition and catalysis. Trends Pharmacol Sci 2002;23:281–287. [PubMed: 12084634]

53. Hu J, Barbour LJ, Gokel GW. The indole side chain of tryptophan as a versatile pi-donor. J Am Chem Soc 2002;124:10940–10941. [PubMed: 12224916]

54. Munshi C, Thiel DJ, Mathews II, Aarhus R, Walseth TF, Lee HC. Characterization of the active site of ADP-ribosyl cyclase. J Biol Chem 1999;274:30770–30777. [PubMed: 10521467]

55. Zechel DL, Withers SG. Dissection of nucleophilic and acid-base catalysis in glycosidases. Curr Opin Chem Biol 2001;5:643–649. [PubMed: 11738173]

56. Yoshikuni Y, Ferrin TE, Keasling JD. Designed divergent evolution of enzyme function. Nature 2006;440:1078–1082. [PubMed: 16495946]

57. Tarnus C, Muller HM, Schuber F. Chemical evidence in favour of a stabilized oxocarbonium-ion intermediate in the NAD^+ glycohydrolase catalyzed reactions. Bioorg Chem 1988;16:38–51.

A

E + NAD⁺ ⇌ E.NAD⁺ ⇌ (- nicotinamide) E.ADP-ribosyl intermediate

CH₃OH → E + β-methyl-ADP-ribose + H⁺ (methanolysis)

H₂O → E + ADP-ribose + H⁺ (hydrolysis)

E.cADP-ribose

E + cADP-ribose (cyclization)

B

NAD⁺ →

oxocarbenium transition state

ADP-ribosyl reaction intermediate

cADPR

H₂O → ADPR

FIGURE 1.
(A) Minimal kinetic mechanism for reactions catalyzed by ADP-ribosyl cyclase family members. (B) Molecular mechanism of the reaction catalyzed by *Sm*NACE. This hypothetical mechanism was adapted from studies on mammalian CD38. The reaction involves the cleavage of the nicotinamide-ribosyl bond via a late transition state leading to the formation of either a covalent acylal ADP-ribosyl intermediate or a carboxylate-stabilized oxocarbenium ion intermediate. In either case the intermediate is then transformed via competing pathways : i) reaction with water yielding ADP-ribose, or ii) intramolecular cyclization to form cyclic ADP-ribose by reaction of N1 of the adenine ring with the C1'' of the intermediate. The catalytic carboxylate corresponds to Glu[202] in *Sm*NACE. At a molecular/structural level, the precise mechanism by which the 'signature' Glu[124], the second active site carboxylic group, controls the cyclization to hydrolysis ratio remains poorly understood. For a full discussion of the molecular mechanism of these enzymes, see (3).

```
Cyclase_A.cal   QQQLPKNK------------VMFWSGVYDEAHDYANTGRKYITLEDTLPGYMLNSLVWCG   137
CD38_human      TQTVPCNK------------ILLWSRIKDLAHQFTQVQRDMFTLEDTLLGYLADDLTWCG   161
CD157_human     RHSIPRDK-----------SLFWENSHLLVNSFADNTRRFMPLSDVLYGRVADFLSWCR   145
SmNACE          YQLFELEQQQQQRHHTIQTEQYFHSQVMNIIRGMCKRLGVCRSLETTFPGYLFDELNWCN   139
SjNACE          HKTFEMQQQPNQ------SGQYFHSQVTHVIRGMCKRLGVCRSLETTFPGYLFDELDWCN   132

Cyclase_A.cal   QRANPGFNEKVCPDF-KTCPVQARESFWGMASSSYAHSAEGEVTYMVDGSNPKVPAYRPD   196
CD38_human      EFNTSKINYQSCPDWRKDCSNNPVSVFWKTVSRRFAEAACDVVHVMLNGSRSK--IFDKN   219
CD157_human     QKNDSGLDYQSCPTS-EDCENNPVDSFWKRASIQYSKDSSGVIHVMLNGSEPTG-AYPIK   203
SmNACE          GSLTGNTKYG--TVCGCDYKSNVVHAFWQSASAEYARRASGNIFVVLNGSVKA--PFNEN   195
SjNACE          NSLIDSSHYG--TVCKCDYYNGVINAFWKSASAEYARRASGTIFVVLNGSAKL--PFNEN   188

Cyclase_A.cal   SFFGKYELPNLTN-KVTRVKVIVLHRLGEK-IIEKCGAGSLLDLEKLVKAKHFAFDCVEN   254
CD38_human      STFGSVEVHNLQPEKVQTLEAWVIHGGRED-SRDLCQDPTIKELESIISKRNIQFSCKNI   278
CD157_human     GFFADYEIPNLQKEKITRIEIWVMHEIGGP-NVESCGEGSMKVLEKRLKDMGFQYSCIND   262
SmNACE          KTFGKIELPLLKHPRVQQLTVKLVHSLEDVNNRQTCESWSLQELANKLNSVHIPFRCIDD   255
SjNACE          RTFGSVELPQLKYPKVKQLIVKLIHNLEDSIPRHTCESINLLRLSSKVKSSNISFSCIND   248
```

FIGURE 2.
Sequence alignment between *S. mansoni* NACE and representative members of the ADP-ribosyl cyclase family. The amino acid sequence alignment (Clustal W 1.82) of the active site domains reveals the conservation of the invariant catalytic Glu (Glu[202] ; bold) and other important residues of the active site such as Glu[124] (bold) and Trp[165] (shaded). The second invariant Trp residue present in the active site of all other members of the cyclase family (grey shaded) is replaced by His[103] in *Sm*NACE. The 'signature region' TLEDTLLGY (shaded) is present in all known CD38 orthologs.
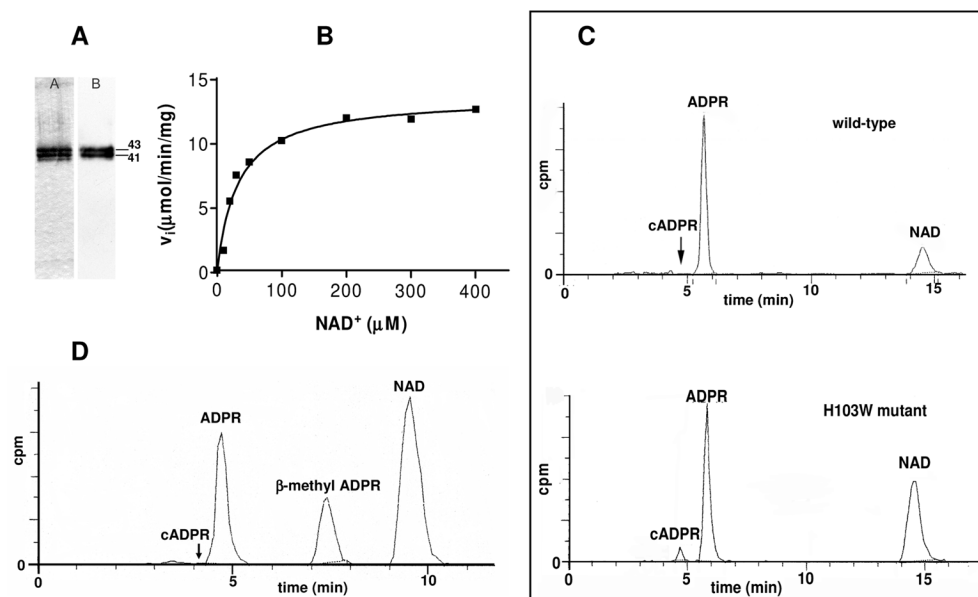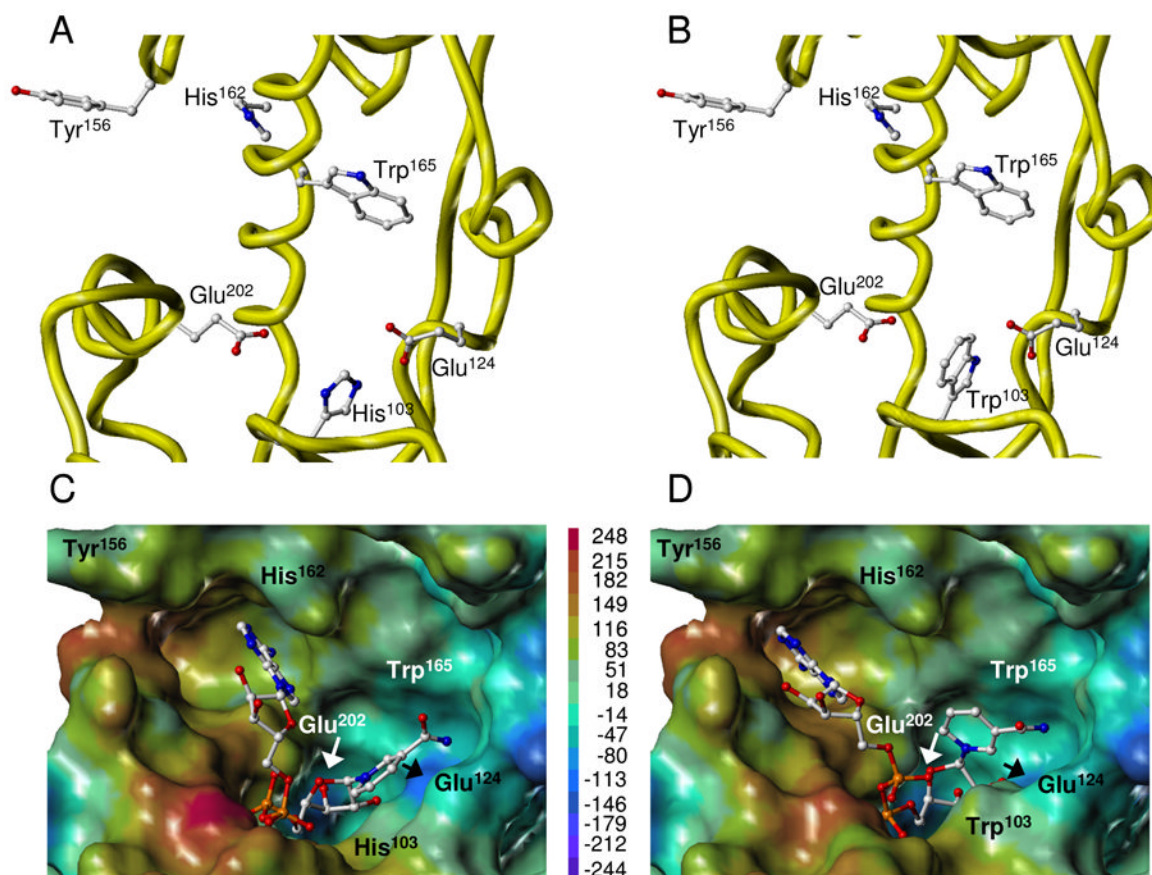
FIGURE 3.
Recombinant soluble H103W *Sm*NACE catalyzed transformation of NAD$^+$. (A) Analysis by SDS-PAGE and Western blotting of purified recombinant H103W *Sm*NACE mutant. Left lane: silver-stained SDS-PAGE gel (12%) – Right lane: immunoblot using anti-NACE antibody (16). The molecular weights (kDa) of the purified mutant are indicated. (B) Kinetics of NAD$^+$ transformation catalyzed by H103W *Sm*NACE mutant. Assays were carried out at 37° C in 10 mM potassium phosphate buffer, pH 7.4. Initial rates were determined at the given substrate concentrations and the data were fitted to the Michaelis-Menten equation. (C) Representative HPLC radiochromatograms of the reaction products observed after transformation of ^{14}C-labeled NAD$^+$ by WT (upper panel) and H103W mutant *Sm*NACE (lower panel). The assays were performed at 37°C in 10 mM potassium phosphate buffer, pH 7.4, in the presence of [^{14}C]NAD$^+$ and the reaction products were monitored by radiodetection. (D) Representative HPLC elution profile of the products obtained by solvolysis of NAD$^+$ catalyzed by the H103W *Sm*NACE mutant in the presence of 3.0 M methanol. The methanolysis peak was identified by co-elution with an authentic sample of β-methyl ADPR (57).
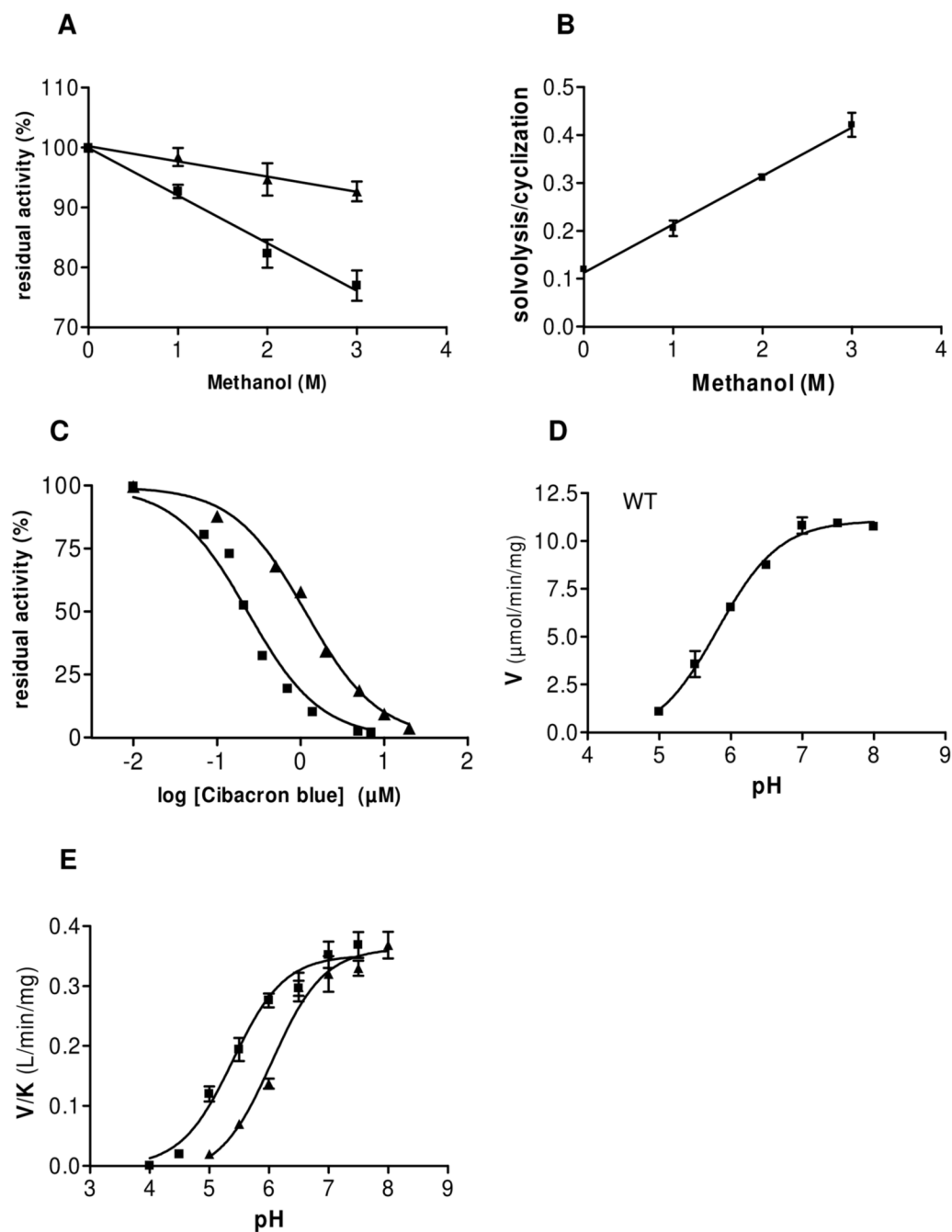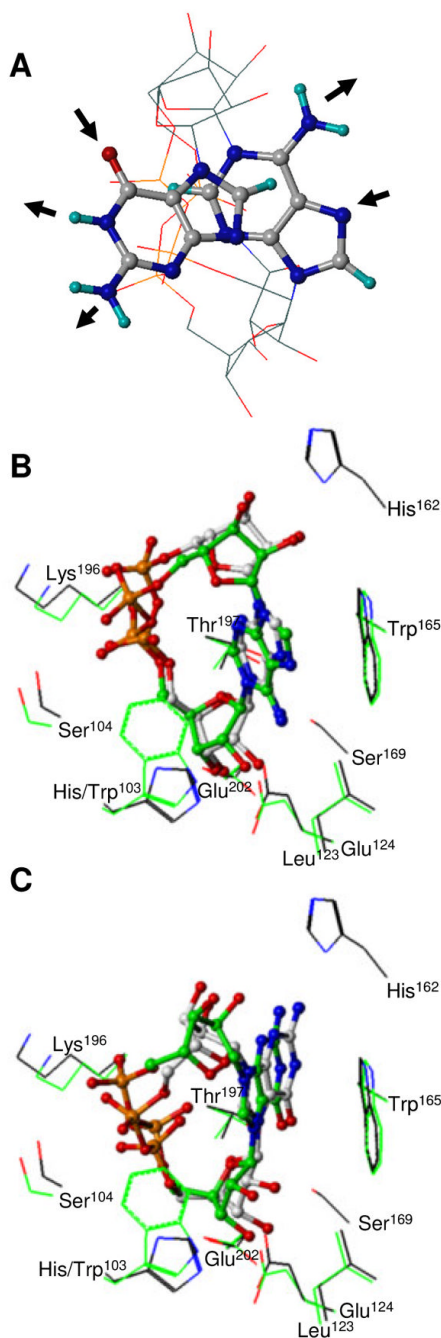
FIGURE 4.
Effect of methanol, Cibacron blue F3GA and pH on reactions catalyzed by *Sm*NACE. (A)
Effect of increasing concentrations of methanol on the rate of transformation of 100 μM
NGD$^+$ into cGDPR catalyzed by WT (squares) and H103W mutant (triangles) of *Sm*NACE.
The assays were carried out at 37°C in 10 mM potassium phosphate buffer, pH 7.4, and the
cyclization reaction progress monitored fluorometrically at λ_{em} = 410 nm (λ_{exc} = 310nm).
Residual activities (means ± SD, *n*=4) are percent of the activity measured in the absence of
solvent. (B) Effect of methanol on the solvolysis/cyclization ratio (= [GDPR + β-methyl
GDPR]/[cGDPR]) observed on transformation of 100 μM NGD$^+$ catalyzed by WT *Sm*NACE
(means ± SD, *n*=3). The reaction products were analyzed by HPLC and their relative

proportions were quantified as described previously (8). (C) Inhibition of WT and H103W *Sm*NACE by Cibacron blue F3GA. The effect of the Cibacron blue on the initial rates of the transformation of 20 μM 1,N^6-etheno-NAD$^+$ catalyzed by *Sm*NACE in 10 mM potassium phosphate buffer, pH 7.4, was followed fluorometrically (λ_{em} = 410 nm; λ_{exc} = 310 nm) at 37° C. The IC$_{50}$ values were calculated from the plot of residual activity against log of dye concentration. WT (triangles) and H103W *Sm*NACE mutant (squares). (D) pH dependence of WT *Sm*NACE. The pH profile of V$_{max}$, measured at 37°C, using 1,N6-etheno-NAD$^+$ as substrate displayed a critical ionization with a pKa of 5.82 ± 0.07 which must be unprotonated for catalytic activity. (E) pH profiles of V$_{max}$/K$_m$ values determined at 37°C using 1,N^6-etheno-NAD$^+$ as substrate (*n* = 3). WT (triangles) and H103W *Sm*NACE mutant (squares). In (D) and (E) the solid lines represent the fit of the data (*n* = 3) to a single pKa model.
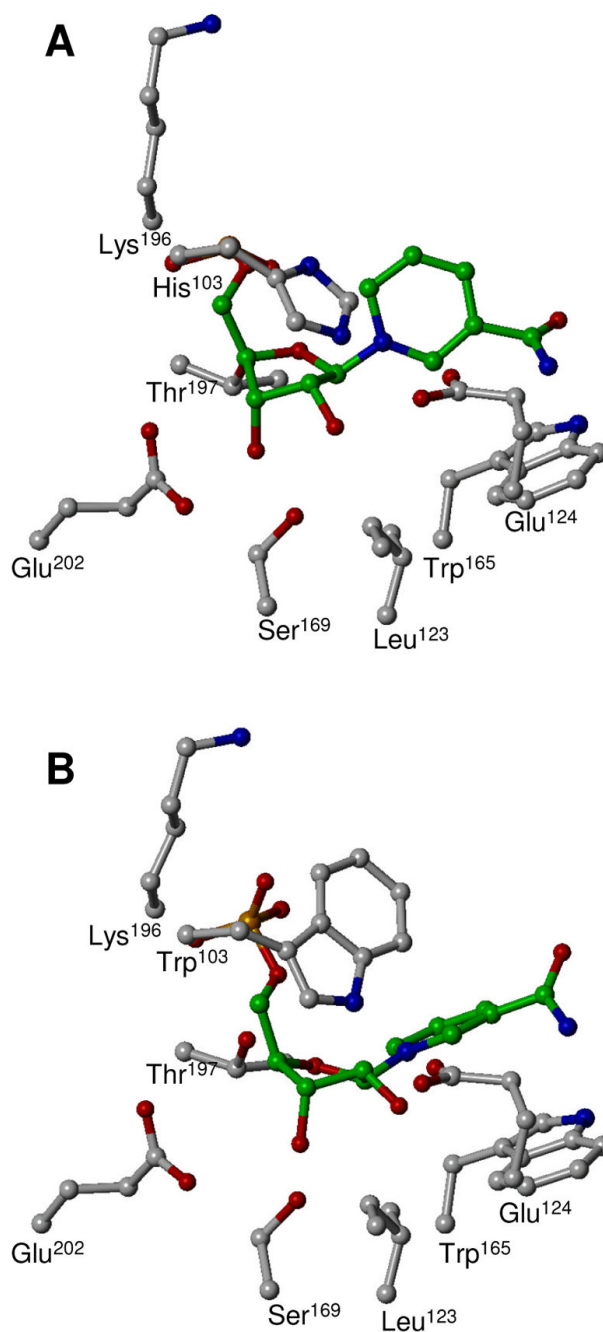
FIGURE 5.
Three-dimensional structure of WT and H103W *Sm*NACE active sites. Free WT (A) and mutant (B) enzymes. Yellow ribbons illustrate the secondary structure elements that form the catalytic cleft. Side chains of the key residues are depicted using ball-and-stick representation and colored by atom type. NAD^+ docked into the active site of WT (C) and mutant (D) enzymes. The best GOLD poses (fitness values of 64 and 82, respectively) of NAD^+ are shown in ball-and-stick and colored by atom type. The active site is represented as Connolly surface and colored according to the electrostatic potential computed using AMBER7 FF99 charges. The color ramp of electrostatic potential (in kcal/mol) ranges from red (most positive) to purple (most negative). The protein is always displayed in the same orientation. The rendering was performed using SYBYL ver. 7.1. Color code : white = C, red = O, dark blue = N, cyan = H and orange = P.

FIGURE 6.
Views of cADPR and cGDPR three-dimensional structure. (A) Free cADPR and cGDPR. Best-fit superposition of the pyrophosphate and ribose heavy atoms of the MacroModel lowest energy conformers. For sake of clarity, ribose and pyrophosphate groups are depicted without hydrogen atoms using line representation whereas all atoms of adenine and guanine bases are shown using ball-and-stick representation. Molecules are colored by atom type as defined in Figure 5. H-bond donors and acceptors in the Watson Crick edge of the bases are indicated using arrows. cADPR (B) and cGDPR (C) docked into the WT and H103W *Sm*NACE active site. Carbon atoms of the WT and mutant complexes are shown in grey and green respectively (the other atoms are colored as defined in Figure 4). All ligand heavy atoms are shown using

ball-and-stick. Side chains of the key residues involved in ligand binding are depicted using a line representation and illustrate the surrounding enzyme structure. The rendering was performed using SYBYL 7.1.

FIGURE 7.
Interaction of the NMN$^+$ moiety of NAD$^+$ docked into the active site of WT (A) and H103W mutant (B) of *Sm*NACE. Heavy atoms of NMN$^+$ and side chains of the enzyme key residues are depicted using ball-and-stick representation. Carbon atoms of NMN$^+$ are colored in green, all the other atoms are colored by atom type as defined in Figure 5. The rendering was performed using SYBYL 7.1. The 'catalytic' Glu^{202} is believed to be involved in the stabilization of the putative oxocarbenium ion transition state formed during the nicotinamide-ribosyl bond cleavage and in the stabilization of the ADP-ribosyl reaction intermediate, see (3). The 'signature' Glu^{124} is taking part in the partitioning of the intermediate between cyclization and hydrolysis.

Table 1

Kinetic parameters for WT and H103W *Sm*NACE

Substrate[a]	*Sm*NACE variant	K_m (μM)	V_{max} (μmol/min/mg)	cyclization[b] (%)
NAD⁺	WT[c]	38.5 ± 6.8	13.2 ± 2.6	~ 0.02
	H103W	32.4 ± 5.4	13.3 ± 0.9	6.8
NGD⁺	WT[c]	23.4 ± 1.1	4.8 ± 0.1	85.0
	H103W	47.7 ± 4.7	11.5 ± 0.4	90.0

[a] All reactions were performed at 37 °C in 10 mM potassium phosphate buffer (pH 7.4) in the presence of purified recombinant WT and H103W *Sm*NACE. The kinetic parameter values were calculated from a nonlinear regression fit to the Michaelis-Menten equation.

[b] Formation of cADPR or cGDPR given as % of total reaction products

[c] Data taken from (16).

Table 2

Predicted pKa values of key residues in the active site of wild type and H103W mutant *Sm*NACE and human CD38

Residue	*Sm*NACE		Human CD38
	pKa (WT)	pKa (H103W)	pKa
Glu (signature)[d]	0.96[a]	5.22[a]	5.78[a]	1.55[b]
Glu (catalytic)[e]	4.25[b]	7.18[a]	7.16[a]	4.75[b]
His[103]	6.35[b]	n.a.[c]	n.a.[c]	n.a.[c]

[a] Empirical calculation using PROPKA.

[b] Calculation based on electrostatic continuum model using dielectric constant values ranging from 2 for the catalytic Glu to 6 for His[103] and the 'signature' Glu.

[c] Not applicable.

[d] Glu[124] and Glu[146] in *Sm*NACE and human CD38, respectively, are part of the 'signature region' of the ADP-ribosyl cyclases.

[e] Glu[202] and Glu[226] in *Sm*NACE and human CD38, respectively.